Estimation of Tissue Elasticity by Image Processing of Simulated B-mode Ultrasound Images

Aidan Constant[†] **and William M. D. Wright**[*]

Department of Electrical & Electronic Engineering
University College Cork,
Cork, IRELAND

[†]aidanc@rennes.ucc.ie [*]bill.wright@ucc.ie

Abstract — **Elastography and strain imaging often use ultrasound to measure mechanical properties of soft tissues. These techniques generally examine radiofrequency signals from an ultrasound scanner. This study investigates the feasibility of strain estimation directly from an ultrasound B-mode image, using segmentation and shape analysis. Several thousand computer generated tissue mimicking phantoms with stiff inclusions were produced and analysed, evaluating the change in shape when the phantom is subjected to 1-D compression in order to estimate strain. The resulting stiffness measurements are accurate to within 8% of the actual values.**

Keywords — **Elastography, Ultrasound B-mode, Shape Analysis, Image Processing.**

I Introduction

Elastography is a well-established technique used to estimate stiffness distribution and other mechanical properties in soft tissues that are subjected to a physical compression. This method usually analyses radiofrequency (RF) signals obtained from an ultrasound scanner and typically employs various cross-correlation techniques to compute the rate of change of tissue displacement, or strain, which in turn is used to calculate the stiffness distribution [1].

Studies have shown that changes in tissue stiffness can be linked to pathological changes i.e. different types of cancers have characteristic ranges for their Young's Modulus value [2]. For example, the elasticity of a nodule serves as an indication of its level of malignancy, cancerous tissue generally being stiffer than benign masses or healthy tissue. Clinicians have often used manual palpation to examine the stiffness of such inclusions in the human breast and prostate. This method is common, but the results are open to user interpretation as a recently published study has shown [3]. Previous palpation studies have also demonstrated that manual measurements of lesion height, width and area in both B-mode and strain images may be used to differentiate between malignant and benign lesions, although of concern was the difficulty in manually tracing lesion boundaries in a busy clinical setting [4][5].

Recently, elastography and other forms of elasticity imaging have used RF signal processing methods and ultrasonic B-mode image processing as a means to automate the palpation process and accurately measure the stiffness of tissue regions [6]. In conventional elastography, compression levels are limited (usually 1mm) due to geometric and material nonlinearities. Large deformations thus require complex non-linear processing of RF signals [7].

Recent work has highlighted the differences in stiffness between malignant and benign growths using ultrasonic shear waves [8]. Such techniques are computationally intensive as the entire image must be processed and access to the raw RF ultrasonic signals is also required. In addition, small levels (<2%) of strain are required to prevent phase wraparound and aliasing in the image, requiring significant subsampling and making the results more susceptible to error. Hence, a more targeted approach could lead to significant reductions in computational requirements.

This work was funded by IRCSET under the Embark Initiative Postgraduate Scholarship Scheme

The lesions are usually located in advance of conventional elastography using B-mode ultrasound imaging, and whilst a significant body of work is devoted to imaging low contrast lesions such as those produced by HIFU (High Intensity Focused Ultrasound) heating, the size and shape of the target is usually known and this information may be used in a straightforward technique to determine the tissue stiffness.

The method being explored in this work utilises image segmentation and shape fitting techniques rather than RF signal analysis to evaluate the change in shape of a tissue mass as it is deformed under a mechanical compression. Provided that the tissue mass is visible, such a change in shape can be determined solely from the B-mode image in the ultrasound scanner and thus the need for analysis of the raw RF signal data to produce an elasticity image can be eliminated.

The work described here examines the feasibility of using an automated shape fitting algorithm and associated image processing methods to evaluate tissue stiffness and hence malignancy. Since this technique does not make use of cross-correlation, and looks only at the final image being generated, the compression limit for elastography does not apply, hence much larger practical deformations can be applied to the tissue sample. Larger deformations produce a more pronounced change in shape, thus simplifying the strain estimation process. In addition to this, making use of large compressions eliminates the need for precision equipment required to introduce small compressions to a tissue sample.

Shape fitting algorithms are used here to determine the outline of the tissue mass within the conventional B-mode image, and then the deformation of this shape under various levels of strain, up to approximately 25%, are used to estimate the stiffness of the tissue.

II Simulation

Computer models of homogenous tissue mimicking phantoms with stiff cylindrical inclusions were generated with Matlab. These were modelled as an array of 12,000 randomly positioned ultrasound scatterers within specified dimensions *(x, y, z) = (50mm, 10mm, 50mm)*. The scatterers were assigned random amplitudes based on a Gaussian distribution. The amplitude of each scatterer within the stiff inclusion was multiplied by a scattering factor of ten to replicate highly scattering, or hyperechoic, inclusions. One-dimensional compression was applied to each model, reducing its overall height and distorting the shape of the cross section of the inclusion from a circle to an ellipse. The soft tissue was assumed to be incompressible, hence the area of the shape in the image remains constant during compression.

Table 1: Parameter ranges for simulated phantoms

Parameter	**Range of values**
Diameter of inclusion	10mm, 15mm, 20mm
Stiffness contrast between inclusion and background	2:1, 3:1, 4:1, 5:1
Compression/deformation applied to phantom	2, 4, 6, 8, 10, 12, 14 mm (axial direction)
Object location within phantom	Varied arbitrarily

Using Jensen's FIELD II software, a well-validated and established simulator [9], an ESAOTE 8MHz, 30-element, 40mm, linear ultrasound transducer available *in-house* was modelled and used to simulate a B-mode image of each tissue phantom in the *xz*-plane. The phantoms were produced with variations in a number of physical properties such as size, shape and stiffness of inclusions, as well as the degree of deformation applied, as described in Table 1. Each phantom specified was reproduced 50 times so that a statistical analysis could account for any random anomalies in a given phantom. In total, 23,500 (470×50) phantom/image pairs were produced and examined for the statistical study.

III Shape Analysis Algorithm

The goal of the shape analysis algorithm used was to automatically segment the stiff inclusion in the input ultrasonic B-mode frame from the background based on its brightness, texture and size within the image. This was achieved using a combination of techniques including binary thresholding, image filtering, edge detection, texture analysis, distance transforms and mathematical morphology. Once the shape had been segmented, the algorithm measured various dimensions and properties of the shape. The algorithm is detailed below.

a) Image Processing

The original B-mode image was read into memory as a greyscale image (Figure 1(a)). This was converted to a logical image (i.e. a 2-D binary array) through the application of a predefined threshold (Figure 1(b)). Given a greyscale image *I(x, y)* and a threshold level θ, the binary image *B(x, y)* is computed as follows:

$$B(x,y) = \begin{cases} 1, & I(x,y) > \theta \\ 0, & I(x,y) \leq \theta \end{cases} \quad (1)$$

In this binary image, the black foreground pixels were not clearly separated from the background regions. The object in the centre of the frame

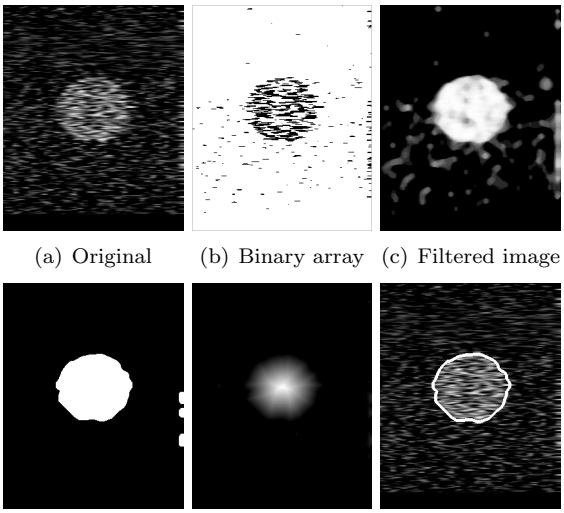

(a) Original (b) Binary array (c) Filtered image

(d) Thresholded (e) Distance map (f) Object outline

Fig. 1: Image processing stages

consisted of a mixture of black and white pixels (approx. 50%–50%), while there were still many small black regions spread out over the entire image, which could be misinterpreted as part of the foreground object and as such needed to be eliminated. This effect was a result of the ultrasound scatterers, which were randomly placed throughout the phantom. However, despite the haphazard appearance of these background fluctuations, the texture was quite consistent and the application of an entropy filter served to further differentiate the "mixed" nature of the foreground region when compared to the more regular colour of the background. This filter traversed the image and assigned to each pixel the value of the entropy of the 9×9 neighbourhood region that surrounded it. Entropy is a statistical measure of randomness in the image, described by:

$$e = -\sum_{i=0}^{L-1} p(z_i) \log_2 p(z_i) \tag{2}$$

where *p(z)* is the histogram of brightness levels in the region and L is the number of possible intensity levels in the image (e.g. 2 in a binary image, 256 in an 8-bit greyscale image) [10]. By applying a 13×13 median filter [10] to the entropy-filtered image (which smoothed the noise in the image while preserving any shapes) it can be seen (Figure 1(c)) that the background now had a much more consistent appearance to it than in the original. The image was again thresholded, resulting in a binary image that clearly distinguished between foreground and background regions in the image. However, in this representation, the object region was generally found to have minor segments protruding from its outer edges. To remedy this, the resultant binary image was morphologically opened, as in Figure 1(d), which also removed any small unwanted white pixels from the background. The morphological opening [11] performed an *erosion* (shrinking) followed by a *dilation* (expansion) using a circular structuring element with a diameter of 7 pixels. Mathematically, the dilation of a binary image B by a structuring element S is based on Minkowsky addition [12] and is defined as:

$$B \oplus S = \bigcup_{t \in S} B_t, \quad B_t = \{b + t | b \in B\} \tag{3}$$

where B_t is the translation of B by a movement vector t. Erosion, or Minkowsky subtraction [12], can be thought of as the opposite action to dilation (although the two are not commutative) and can be defined as follows:

$$B \ominus S = \bigcap_{t \in S} B_t, \quad B_t = \{b + t | b \in B\} \tag{4}$$

Morphological opening is thus defined as [13]:

$$B \circ S = (B \ominus S) \oplus S \tag{5}$$

b) Shape Analysis

From the logical image in Figure 1(d) a label matrix was created using connected component labelling [13] with 4-point connectivity, and the Euclidean distance transform was also computed [14]. A label matrix was produced from the binary image by grouping all connected pixels into objects and allocating a label to each object, assigning the value of the object label to all pixels within that object. The distance transform creates a Euclidean distance map in which the value of each pixel represents the straight line distance from that pixel to the nearest boundary point, calculated using a Euclidean metric i.e. given two points *(x_a, y_a)* and *(x_b, y_b)*, the Euclidean distance D_E is computed from Equation 6.

$$D_E = \sqrt{(x_a - x_b)^2 + (y_a - y_b)^2} \tag{6}$$

The output from the distance transform provided an indication of the location of the largest object in the image (Figure 1(e)). Using these results the image processing algorithm performed an iterative search on the labelled regions in the matrix in order to find the largest object that was entirely contained within the borders of the image. This was achieved by locating the maximum of the distance transform and ensuring that it was above an acceptable threshold, which indicated if a sufficiently large object had been detected. This location was then referenced in the label matrix and should coincide with one of the labelled areas, identifying the region of interest. If this region intersected the perimeter of the image, it was

deemed unsuitable as the entire object may not be visible in the image. In this case, the object was removed from the matrix, the distance transform was recomputed and the process repeated until a sufficiently large object was found that was fully contained within the image boundaries or when the maximum of the distance transform was below the acceptable threshold (i.e. remaining regions were too small and the algorithm failed). The advantage of using the distance transform in this manner is that it will usually select the object on the first iteration, but it is still robust enough to ignore any undesired regions in the image.

When the desired region in the label matrix had been identified, all other regions were removed and the label matrix was simplified to a binary image containing a single foreground object. The outline of the shape was determined using Sobel edge detection [15], as shown in Figure 1(f). Various shape parameters of this foreground object were subsequently measured, including area, centroid, height, width, bounding box, and then stored for calculation of the strain.

The 1-D strain calculation focused on the height of a detected region before (h_{pre}) and after (h_{post}) compression of the phantom, height being measured as the distance between the upper and lower extreme points of the target shape. The strain ε of the observed object can thus be computed from Equation 7. Young's modulus, or stiffness, is the ratio of stress to strain. Therefore if it is assumed that there is a constant stress throughout the tissue sample, then the reciprocal of the calculated strain provides a good indication of stiffness.

$$\varepsilon = \frac{h_{post} - h_{pre}}{h_{pre}} = \frac{\Delta h}{h_{pre}} \tag{7}$$

For each phantom where a deformation was applied, the height measurement h_{post} was compared to that from the corresponding uncompressed phantom h_{pre} and these values were used to calculate strain in the object as in Equation 7.

Figure 2 shows an example of increasing levels of compression being applied to a computer generated phantom. The phantom in question contained a 20mm diameter cylindrical hyperechoic inclusion, with a Young's modulus three times stiffer than that of the background tissue. As the compression was increased, the overall height of the phantom decreased (as can be seen from the thickening black band across the bottom of the images) and the inclusion was also distorted, with an increasing width to compensate for the decrease in height (i.e. area was conserved). Note that the images in Figure 2 are of four different phantoms, since each phantom was individually created from a series of random ultrasound scatterers. This explains why the general outline of the inclusion changes from frame to frame, and also illustrates the robustness of the algorithm in successfully analysing a host of different phantom images.

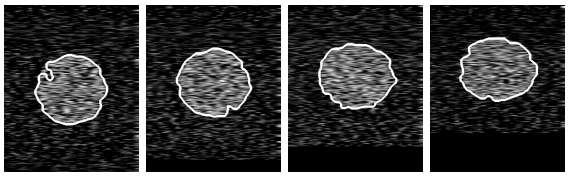

(a) 0mm (b) 4mm (c) 8mm (d) 12mm

Fig. 2: Increasing levels of compression

IV Data Analysis

The image processing algorithm detailed above was applied to all simulated images and height measurements were taken for the inclusions in each phantom. The error in this height measurement was calculated as the difference between the measured value and the actual physical dimension from the phantom parameter specifications. For the three inclusion sizes that were inspected (10mm, 15mm, 20mm diameter), this measurement error was plotted against the amount of deformation applied (the mean error was computed for each compression level [0, 2, 4, ... 12, 14 mm]). A linear trend line was fitted to each of the three plots. The results are plotted in Figure 3. This error formula was then used to adjust the heights obtained in order to compensate for any measurement error that occurred.

$$h_{adj} = h_{meas} - y\,(x) \tag{8}$$

The measured compression Δh from Equation 7 was computed for each image and plotted as a function of the actual compression of the object in each phantom (a separate plot was obtained for

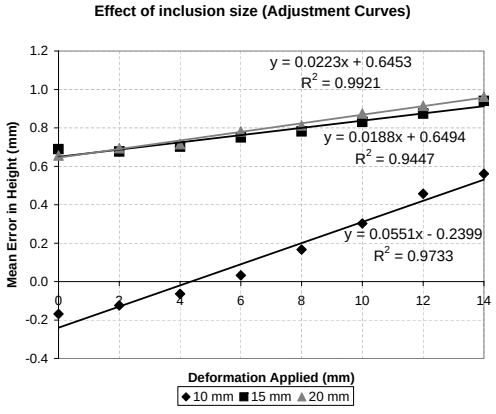

Fig. 3: Trend lines fitted to error data showing effect of inclusion size on measurements

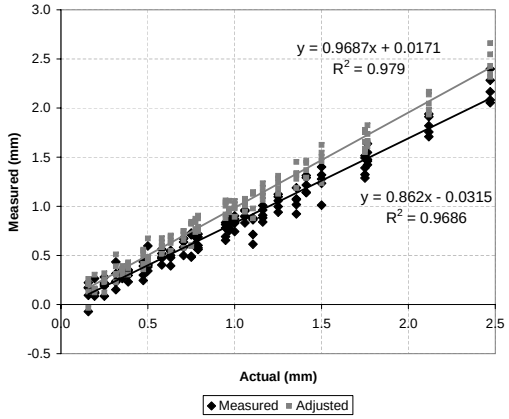

Fig. 4: Measured vs. actual compression

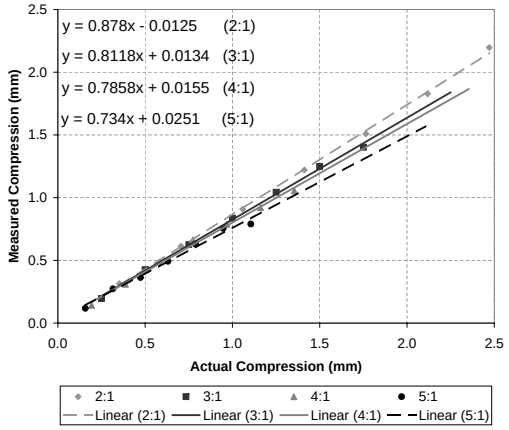

Fig. 5: Measurement variation with increasing stiffness contrast

each of the three inclusion sizes), which produced three scatter plots, one of which is shown in Figure 4 (15mm objects). When the original height data were adjusted for measurement error, Δh was recomputed and the plots redrawn (overlaid in Figure 4).

The measured data were also investigated for trends based on the foreground-to-background stiffness contrast ratio in the phantoms. The data were separated into four groups based on stiffness contrast and a line was fitted to each data set, as in Figure 5.

V Results

The adjustment curves plotted in Figure 3 exhibit a high degree of similarity for the 15mm and 20mm inclusions. The slopes for these two trend lines are comparable (0.0188 and 0.0223) and there is a relatively constant offset of approximately 0.65mm. This offset is due to the nature of the individual ultrasound scatterers and their appearance in the B-mode images. The size of each scatterer is not significant when compared to the size of the inclusions. However, this is not the case with the 10mm images, where the detected shapes are quite small relative to the overall image size and thus the image analysis algorithm does not depict these as accurately as the larger shapes. Hence, the slope of the adjustment curve is steeper (0.0551) and the 0.65mm offset is overshadowed by the less precise shape outlines.

Table 2: Trend lines fitted to measurement data

	Diam.	Equation	R^2
Orig. data	10mm	y = 0.4384x - 0.0670	0.4149
	15mm	y = 0.8620x - 0.0315	0.9686
	20mm	y = 0.8913x + 0.0213	0.9735
Adj. data	10mm	y = 0.9266x + 0.0863	0.8525
	15mm	y = 0.9687x + 0.0171	0.9790
	20mm	y = 0.9823x + 0.0737	0.9791

Figure 4 shows the measured compression versus actual compression for all phantoms with 15mm diameter inclusions. Note that each point in the graph represents a mean value from the 50 phantoms with similar statistical properties (each phantom was reproduced 50 times to avoid any statistical anomalies). Similar plots were also produced for the 10mm and 20mm diameter objects. The linear trend line equations are displayed in Table 2 for both the original and corrected data, along with the corresponding R-squared value indicating how well the line approximates the data. It is clear from Table 2 that when the measurements were adjusted, a marked improvement was observed in the representation of the physical data using the image analysis technique. The slopes of the three lines, and hence the accuracy of the height measurements, were increased from 0.4384 to 0.9266 (10mm), 0.862 to 0.9687 (15mm) and 0.8913 to 0.9823 (20mm) after compensation. This means that the measured data can be used to estimate the strain of the target objects to within 8% (10mm), 4% (15mm) and 2% (20mm). R-squared values for these trend lines were 0.8525 (10mm), 0.9790 (15mm) and 0.9791 (20mm), indicating good correlation. These results are equivalent to those obtained in [8], but were arrived at using less computationally intensive means.

From the results plotted in Figure 5 there is a slight decrease in slope with increasing stiffness contrast in the phantoms. The slopes vary from 0.878 (2:1) down to 0.734 (5:1), as compared to the original value of 0.862 before the data was divided into subgroups. This is because for a given level of applied deformation, stiffer tissue masses will compress less, increasing the measurement error.

The use of simulated images allowed many different phantom parameters (e.g. inclusion size, stiffness ratio, scatterer density) and other test parameters (e.g. compression level, threshold values)

to be varied to fully evaluate the robustness of the algorithm, and only a fraction of the results is presented here. Real data acquisition from agar and gelatin based tissue phantoms is currently under investigation.

VI Conclusions

In this paper a method of estimating the stiffness of hard inclusions in soft tissue through shape analysis in an ultrasound B-mode image was investigated. The feasibility of this process was evaluated using a large scale simulation and statistical study.

A linear relationship was established between the data measured from the images and the actual physical dimensions of the phantoms. Although the data contained some measurement errors, this was easily modelled and compensated for to produce an accurate representation of the phantom dimensions from the B-mode images. These errors were found to be relatively constant and predictable for all inclusions, provided the area of the examined shape was not too small relative to the overall image size (as was the case with 10mm diameter lesions). Trends in the ratio of foreground to background Young's modulus (stiffness) were also examined. Slightly larger measurement errors were observed for higher stiffness contrasts but these were found not to have a great effect on the overall results.

With the corrected height measurements accurately depicting real height of the objects in the compressed phantoms, the algorithm detailed in this study can now be used to measure strain from ultrasound B-mode images of phantoms undergoing 1-D compression to within 8% of the actual value, although this can be reduced to 4% if the smallest objects are ignored.

References

[1] J. Ophir, I. Cespedes, H. Ponnekanti, Y. Yadzi, and X. Li, "Elastography: a quantitative method for imaging the elasticity of biological tissues," *Ultrason Imaging*, vol. 13, pp. 111–134, 1991.

[2] W. Anderson, *Pathology*. Mosby, 1953.

[3] M. M. Doyley, J. C. Bamber, F. Fuechsela, and N. L. Bush, "A freehand elastographic imaging approach for clinical breast imaging: system development and performance evaluation," *Ultrasound Med Biol*, vol. 27, pp. 1347–1357, 2001.

[4] D. M. Regner, G. K. Hesley, N. J. Hangiandreou, M. J. Morton, M. R. Nordland, D. D. Meixner, T. J. Hall, M. A. Farrell, J. N. Mandrekar, W. S. Harmsen, and J. W. Charboneau, "Breast lesions: evaluation with us strain imaging - clinical experience of multiple observers," *Radiology*, vol. 238, pp. 425–437, 2006.

[5] H. Zhi, B. Ou, B.-M. Luo, X. Feng, Y.-L. Wen, and H.-Y. Yang, "Comparison of ultrasound elastography, mammography, and sonography in the diagnosis of solid breast lesions," *J Ultrasound Med*, vol. 26, pp. 807–815, 2007.

[6] K. Nightingale, M. Scott-Soo, M. Palmeri, A. Congdon, K. Frinkley, and G. Trahey, "Imaging tissue mechanical properties using impulsive acoustic radiation force," *IEEE International Symposium on Biomedical Imaging: From Nano to Macro*, vol. 1, pp. 41–44, 2004.

[7] A. R. Skovoroda, M. A. Lubinski, S. Y. Emelianov, and M. O'Donnell, "Reconstructive elasticity imaging for large deformations," *IEEE Trans Ultrason Ferroelec Freq Control*, vol. 46, pp. 523–535, 1999.

[8] J. Bercoff, A. Criton, C. Cohen-Bacrie, J. Souquet, M. Tanter, T. Deffieux, J. L. Gennisson, M. Fink, V. Juhan, A. Colavolpe, D. Amy, and A. Athanasiou, "Shearwave elastography: a new real time ultrasound imaging mode for assessing quantitatively soft tissue viscoelasticity," *Proc IEEE Ultrason Symp*, pp. 321–324, 2008.

[9] J. A. Jensen, "Field: A program for simulating ultrasound systems," *Medical & Biological Engineering & Computing*, vol. 34, pp. 351–353, 1996.

[10] R. C. Gonzalez, R. E. Woods, and S. L. Eddins, *Digital Image Processing using MATLAB*. Prentice Hall, 2004.

[11] M. Petrou and P. G. Sevilla, *Image processing: dealing with texture*. John Wiley & Sons, Ltd., 2006.

[12] P. K. Ghosh, "A mathematical model for shape description using minkowski operators," *Computer Vision, Graphics, and Image Processing*, vol. 44, pp. 239–269, 1988.

[13] L. G. Shapiro and G. C. Stockman, *Computer Vision*. Prentice Hall, 2001.

[14] P.-E. Danielsson, "Euclidean distance mapping," *Computer Graphics and Image Processing*, vol. 14, pp. 227–248, 1980.

[15] T. Acharya and A. K. Ray, *Image Processing: Principles and Applications*. John Wiley & Sons, Inc., 2005.